

**Bulk motion of granular matter in an agitated cylindrical bed**

Phanikumar Sistla,<sup>1</sup> Oleh Baran,<sup>2</sup> Q. Chen,<sup>1</sup> Stephane Fohanno,<sup>1</sup> Peter H. Poole,<sup>2,3</sup> and Robert J. Martinuzzi<sup>1</sup>  
<sup>1</sup>*Department of Mechanical and Materials Engineering, University of Western Ontario, London, Ontario, Canada N6A 5B9*  
<sup>2</sup>*Department of Applied Mathematics, University of Western Ontario, London, Ontario, Canada N6A 5B7*  
<sup>3</sup>*Department of Physics, St. Francis Xavier University, Antigonish, Nova Scotia, Canada B2G 2W5*  
 (Received 17 February 2004; published 18 January 2005)

Experimental results are reported for the bulk motion induced in a bed of granular matter contained in a cylindrical pan with a flat bottom subjected to simultaneous vertical and horizontal vibrations. The motion in space of the moving pan is quantified. A number of distinct bulk dynamical modes are observed in which the particle bed adopts different shapes and motions. At the lowest pan excitation frequency  $\omega$ , the bed forms a “heap,” and rotates about the cylinder axis. As  $\omega$  is increased, a more complex “toroidal” mode appears in which the bed takes the shape of a torus; in this mode, circulation occurs both about the cylinder axis, and also radially, with particles moving from the outer edge of the pan to the center on the top surface of the bed, and back to the outer edge along the pan bottom. At the highest  $\omega$ , surface modulations (“surface waves” and “sectors”) of the toroidal mode occur. The origin of this family of behavior in terms of the pan motion is discussed.

DOI: 10.1103/PhysRevE.71.011303

PACS number(s): 45.70.-n, 45.70.Mg

**I. INTRODUCTION**

Granular materials play an important role in many industrial processes. In applications, granular materials are often subjected to vibrations to generate material transport, mixing, or size segregation. Consequently, the fundamental properties and motions of granular matter confined to a vibrating container have been widely studied. Many fundamental studies have focused on the motion of particle beds in a rectangular container (the pan). Typically, the bed is excited by pan vibrations along a single axis. Reviews of such studies can be found in Refs. [1–6]. Agitated beds of granular matter have been observed to adopt a wide spectrum of shapes and motions, such as heaping, convection, small amplitude wave motion, arching, and large amplitude wave motion; see, e.g., Ref. [7]. These modes certainly depend on the nature of the vibrations. However, their dependence on the pan geometry is less well understood. For example, in the case of purely vertical vibrations, the effect of the pan shape is absent or weak [8], but this is unlikely to be generally true in the presence of horizontal vibrations.

The motions observed in a cylindrical pan subjected to simultaneous horizontal and vertical vibrations are reported in the present study. There are two principal motivations for studying this case. First, the response of a bed of granular matter to excitations occurring simultaneously along three Cartesian axes has not been extensively studied and remains poorly understood. However, in many industrial applications, triaxial excitations are highly desirable to optimize process parameters. Many fundamental studies have been made of systems subjected to purely vertical or horizontal vibrations, but in only a few cases are vibrations in both directions addressed. An example is the work of Tennekoon and Behringer [9], who reported that when granular matter is subjected to simultaneous horizontal and vertical sinusoidal vibrations, the phase difference between the components of vibration in the two directions becomes a key control parameter for the resulting motion. A quantitative understanding of

the effect of such combined vibrations is therefore important for predicting and controlling the behavior of agitated beds in real applications.

A second motivation is to study the motion generated in a container of cylindrical symmetry, with the cylinder axis oriented vertically. Again, this geometry is common in industrial devices such as sifting machinery, yet is less well studied in a research context compared to square and rectangular geometries. Note that the present case is distinct, both in motion and in orientation, from the more widely studied case of a continuously rotating drum having the cylinder axis oriented horizontally.

A cylindrical geometry provides the opportunity to study phenomena unlikely to occur in the rectangular case. In particular, the absence of discontinuities (i.e., sharp corners) on the vertical boundaries of a cylindrical pan makes possible smooth circulatory motions of the agitated bed. These circulation modes are of interest for applications involving sifting and mixing, and for developing agitated bed devices for continuous, as opposed to batch, processing. Initial studies have also demonstrated that these modes may display complex behavior. For example, Scherer *et al.* [10] have reported that when spheres are placed in a cylindrical pan and are subjected to horizontal shaking, they circulate in one direction at low packing densities, and in the other at high packing densities or high excitation frequencies.

**II. EXPERIMENTAL SETUP**

The agitated bed apparatus studied here (Figs. 1 and 2) is a modified SWECO finishing mill model ZS30S66, a commercially available device widely used in industrial applications for sieving and polishing. It consists of a rigid, circular, stainless steel pan of radius  $R=0.381$  m with a flat bottom. The pan “floats” on an array of nine springs spaced equidistantly around the circumference of the pan bottom. Vibrations are excited by a 0.5 hp motor mounted below the center of the pan.

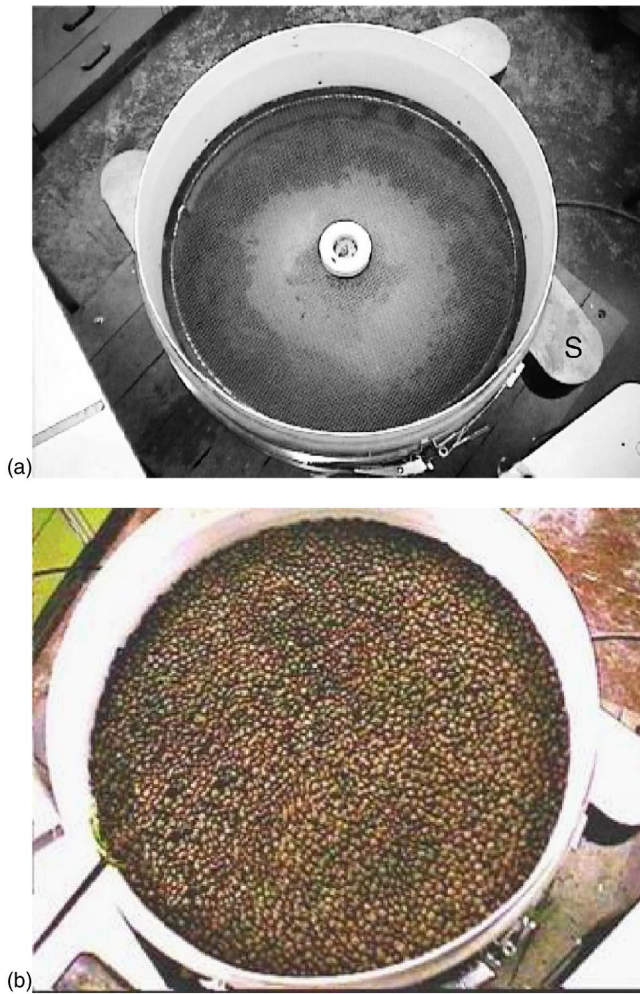


FIG. 1. Photographs of the agitated bed apparatus, viewed from above: (a) without particles; (b) with particles. The location of the spout in (a) is labeled with an “S.”

In order to induce simultaneous horizontal and vertical vibrations, and concurrently obtain control over their relative magnitudes, metal weights are mounted eccentrically at the top and bottom ends of a shaft running through the center of the motor. The motor housing is rigidly attached to the pan via a flange, while the shaft rotates freely with respect to the pan. When the shaft rotates, the effect of the weights is to impose an oscillatory torque that tends to make the motor shaft deviate from the vertical. The effect of this torque is to cause the center of the pan to revolve about a vertical axis, and simultaneously cause the bottom of the pan to deviate from the horizontal. A complete description of the pan motion is given in the next section. The angle between the top and bottom weights, referred to here as the “lead angle”  $\phi$ , can be varied from  $0^\circ$  to  $180^\circ$  [Fig. 2(b)]. Measurements and visualizations are carried out for motor shaft rotational frequencies  $\omega$  in the range from 10 to 20 Hz. While some visualization-only studies are conducted above and below this range, it should be noted that for  $\omega$  below 10 Hz, resonant modes of the pan-spring-bed system are approached, and complex, chaoticlike motions sometimes develop.

The bottom surface of the pan is a stiff, stainless steel sieve. The particles used in this study are too large to fall

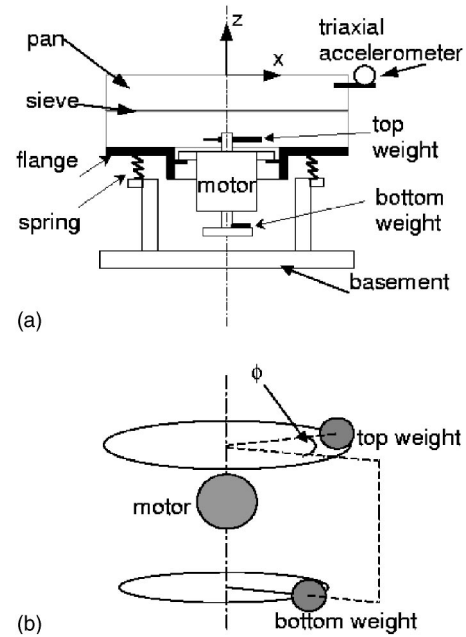


FIG. 2. (a) A schematic view of the apparatus. (b) Schematic representation of the relative positions of the motor and top and bottom weights, and the definition of  $\phi$ .

through the holes of the sieve. The springs that bear the load of the entire pan-motor assembly are mounted on a rigid basement. Note also that there is a cylindrical “hub” attached to the center of the pan bottom, of radius 10.4 cm and height 3.0 cm.

The masses of the top and bottom weights attached to the motor are fixed in this study. As will be shown in the next section, the angle  $\phi$  between the weights controls the ratio of the amplitudes of the horizontal and vertical vibrations imparted to the pan. The rotational frequency  $\omega$  of the motor controls the amount of energy introduced into the system. The principal control parameters for the experiments described here are thus  $\phi$  and  $\omega$ .

The experiments are conducted with two sets of particles: “pill-shaped” oblate spheroid particles, and spherical particles. The oblate spheroids have a major axis of 13.5 mm and a minor axis of 7 mm, a mass of 0.9 g, and a density of  $1200 \text{ kg/m}^3$ , with a hard and smooth polished surface [11]. The spheres are made of nylon [12], are 11.1 mm in diameter, have the same volume as the oblate spheroids, a density of  $1100 \text{ kg/m}^3$ , and a hard, smooth, but unpolished surface. Although the qualitative behavior observed in both cases is similar, it is found that the shape of the particles influences some quantitative properties of the motion. Thus the results obtained with each type of particle are presented separately.

The mass of the unloaded pan is approximately 150 kg. All tests are conducted for particle bed loads below 45 kg and, as shown in the next section, it is found that the influence of the bed load on the pan motion is negligible. Also, it is confirmed in all tests that the pan moves as a rigid body. With 45 kg of particles in the pan, the particle bed (at rest) is about 12 layers deep. The results described below are qualitatively unchanged for particle loads between 15 and 45 kg, i.e., for bed heights in the range between 4 and 12 layers.

The motion of the pan is monitored using Entran accelerometers: one triaxial (model EGA3-F-10-/5) and three mono-axial (model EGA-F-10-/5) units are used. The location of the triaxial accelerometer is shown in Fig. 2; the others are positioned at various locations along the top edge of the pan, according to the degree of freedom to be measured. The accelerometer data are collected using a computer-based data acquisition system and processed to obtain the velocity, displacement, and phase-shift data for the pan motion. A sampling frequency of 2 kHz is used for data acquisition, allowing a minimum resolution of 165 points/cycle. This results in an error in the phase angle measurements of  $\pm 3^\circ$ . The uncertainties in the acceleration and bed displacement are estimated to be  $\pm 0.1g$  and  $\pm 0.05$  mm, respectively, where  $g$  is the acceleration due to gravity. The above uncertainty includes the influence of “cross-axis” acceleration (typically 2% to 3%). It has been verified that this influence is negligible for the analysis. We have also confirmed some of the qualitative aspects of the pan motion using a high speed (500 frames/s) camera.

The surface motion of the particle bed is studied by visually tracking particles. Differently colored particles are used to obtain information on the average mixing time. For the most interesting modes of motion, a localized group of particles is coated with a fluorescent dye and the subsequent motion of this group is recorded photographically. The dye is sodium fluorescein, which is excited using an ultraviolet light source and observed in the 532 nm visual range.

The results of the experiments are presented in two stages. First, a quantification of the pan motion is presented in Sec. III. Then the modes of particle motion that are observed in the bed are described in Sec. IV.

### III. PAN MOTION

As described above, the experimental apparatus is a commercially available unit that generates simultaneous horizontal and vertical vibrations of the pan. The first task of the present study is therefore to quantify the motion generated by this device. To achieve this, two coordinate systems are defined: one fixed with respect to the pan (the “pan frame”), and one fixed with respect to the laboratory (the “lab frame”).

The intersection of the cylinder axis of the pan with the plane defined by the top edge of the pan is chosen as the origin of a right-handed Cartesian coordinate system  $(x_p, y_p, z_p)$  fixed in the pan frame. The cylindrical symmetry of the pan is broken by the existence of a spout located at a point on the circumference of the pan. The  $x_p$  axis in the pan frame is thus defined as the line that passes through the origin and the location on the spout where the triaxial accelerometer is mounted. The  $y_p$  axis is the line perpendicular to the  $x_p$  axis in the plane defined by the top edge of the pan, and the  $z_p$  axis is perpendicular to both the  $x_p$  and  $y_p$  axes. The Cartesian coordinate system  $(x, y, z)$  in the lab frame is defined as that which is coincident with the pan frame when the apparatus is at rest.

The accelerometers provide data that are analyzed to give the lab frame coordinates as a function of time for points

fixed in the pan frame. To specify the motion of the pan, in the following attention is restricted to points fixed in the pan frame lying in the  $z_p=0$  plane, since this is the plane in which the accelerometers are located. Based on the accelerometer data, the motion in the lab frame of such a point is found to be consistent, within the error of measurement, with the following model:

$$x(t) = x_p + x_{\max} \cos(\Omega t), \quad (1)$$

$$y(t) = y_p + y_{\max} \cos(\Omega t + \alpha_{xy}), \quad (2)$$

$$z(t) = A(r_p) \cos(\Omega t + \alpha_{xz} - \theta), \quad (3)$$

where  $\Omega = 2\pi\omega$ ,

$$A(r_p) = \frac{r_p}{R} z_{\max} \quad (4)$$

and

$$r_p = \sqrt{x_p^2 + y_p^2}. \quad (5)$$

In the above equations,  $x_{\max}$  and  $y_{\max}$  are the amplitudes of the  $x$  and  $y$  displacements of the pan-frame origin in the lab frame;  $\alpha_{xy}$  is the phase shift between the  $x$  and  $y$  displacements in the lab frame; and  $\theta$  is the angle measured about the origin from the  $x_p$  axis to the point  $(x_p, y_p)$ .  $\alpha_{xz}$  is the phase shift between the  $x$  and  $z$  displacements in the lab frame, as measured on the  $x_p$  axis; thus  $(\alpha_{xz} - \theta)$  is the phase shift between the  $x$  and  $z$  displacements in the lab frame, to be found at the point  $(x_p, y_p)$ .  $A(r_p)$  is the amplitude of the  $z$  displacement of a point in the  $z_p=0$  plane that is a distance  $r_p$  from the origin in the pan frame.  $R=0.381$  m is the distance from the origin in the pan frame to the edge of the pan, and  $z_{\max}$  is the amplitude of the  $z$  displacement of a point on the edge of the pan (i.e., at  $r_p=R$ ).

The form of Eqs. (1) and (2) is motivated by the observation that under all operating conditions, the center of the pan appears to execute an approximately circular orbit in a horizontal plane. To visualize this, a laser source is mounted at the center of the pan, pointing upward, normal to the pan bottom. The motion of the pan causes the laser to trace out a pattern on a screen positioned horizontally above the apparatus. Time-exposure photographs of these traces are shown in Fig. 3 for various operating conditions, and are consistent with circular motion of the pan center.

If the motion is nearly circular, the magnitude of the phase shift  $\alpha_{xy}$  should be approximately  $90^\circ$ . This is confirmed in Fig. 4, where  $\alpha_{xy}$  is plotted as a function of  $\phi$  for various  $\omega$ . An apparatus with perfect cylindrical symmetry would have  $\alpha_{xy}=90^\circ$ . Small asymmetries in the apparatus, the most important of which is likely the spout on the edge of the pan [at the location of the triaxial accelerometers in Fig. 2(a)], result in the observed variation in the range  $93^\circ < \alpha_{xy} < 100^\circ$ .

Circular motion of the pan center also requires  $x_{\max}$  and  $y_{\max}$  to be equal. Measurements of  $x_{\max}$  and  $y_{\max}$  at  $r_p=R$  (Fig. 5) show that this is observed to be true within the measurement error across the range of  $\phi$  studied here. Note that as  $\omega$  varies in different test runs,  $x_{\max}$  and  $y_{\max}$  are found

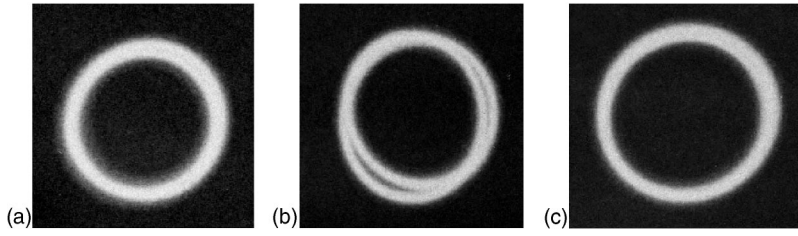


FIG. 3. Photographs of laser traces visualizing the circular motion of the pan center for (a)  $\phi = 10^\circ$ ,  $\omega = 10$  Hz; (b)  $\phi = 60^\circ$ ,  $\omega = 10$  Hz; and (c)  $\phi = 100^\circ$ ,  $\omega = 10$  Hz. The pictures are time exposures of approximately 2 s.

to be scattered around the average values reported in Fig. 5 by about 15%; however, no systematic variation with  $\omega$  can be identified. Tests also show that the values of  $x_{\max}$  and  $y_{\max}$  are independent of the position around the edge of the pan at  $r_p = R$  at which they are measured, consistent with the description in Eqs. (1) and (2). Note that for  $x_{\max}$  or  $y_{\max}$  to have the same measured value independent of  $r_p$  at the point of measurement requires that the tilt angle of the  $z_p = 0$  plane with respect to the  $z = 0$  plane be small. This is confirmed below.

Equation (3) characterizes the tilting motion of the pan by quantifying the vertical deviation of a point fixed in the pan frame (in the  $z_p = 0$  plane) with respect to the  $z = 0$  plane in the lab frame. As in the case of the  $x$  and  $y$  motions, the accelerometer data for  $z(t)$  indicate a sinusoidal function of  $t$ . The form of Eq. (3) also assumes that the origin of the pan frame does not leave the  $z = 0$  plane of the lab frame; this assumption is confirmed by direct visual observation using the high-speed camera. From geometric considerations, the amplitude  $A$  of the  $z$  variation in Eq. (3) is a function of the distance  $r_p$  of the point of measurement from the center of the pan, as indicated in Eq. (4). The phase shift between the  $x$  and  $z$  displacements is a difference of two contributions,  $\alpha_{xz}$  and  $\theta$ .  $\alpha_{xz}$  is the phase shift between the  $x$  and  $z$  displacements as measured on the  $x_p$  axis at  $r_p = R$ .  $\theta$  is a geometrical term that accounts for the difference between the phase shift observed on the  $x_p$  axis and that which would be observed at an arbitrary point  $(x_p, y_p)$  in the  $z_p = 0$  plane. As shown in Fig. 6,  $\alpha_{xz}$  does not depend strongly on  $\omega$ , but does depend on  $\phi$ .

The net effect of the motions described by Eqs. (1)–(3) are summarized in Fig. 7. The motion of the pan can be thought of as a superposition of two motions.

(i) The center of the pan revolves about the lab frame origin in a nearly circular, horizontal orbit. This motion is directly described by Eqs. (1) and (2).

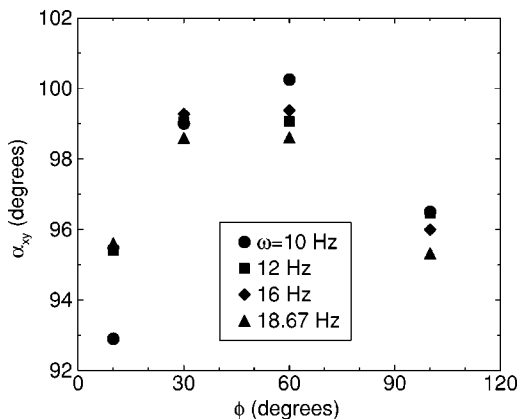


FIG. 4. Phase shift  $\alpha_{xy}$  as a function of  $\phi$  for various  $\omega$ .

(ii) The pan is tilted at an angle  $\gamma$  in such a way that a unit normal vector rooted at the pan center precesses about the vertical at the same frequency at which the center orbits the origin, but phase shifted with respect to the orbital motion of the center. The fact that  $\gamma$  maintains a constant value can be shown from Eq. (3) by considering (e.g.) the case  $r_p = R$  and setting  $\theta = \Omega t + \alpha_{xz}$ . These conditions describe the point on the edge of the pan that at any given  $t$  has the largest positive  $z$  displacement. For all  $t$ , this displacement is a constant,  $z_{\max}$ , and so  $\gamma = \sin^{-1}(z_{\max}/R)$  is also constant. Note that for the apparatus and operating conditions described here,  $R = 0.381$  m, and  $z_{\max}$  is never greater than 0.0035 m, giving  $\gamma < 0.5^\circ$ . This confirms the assumption of small tilt angle required for the chosen form of Eqs. (1) and (2), as indicated above.

The measurements shown in Figs. 4–6 show that both the amplitudes and phase shifts required to specify the pan motion using Eqs. (1)–(3) are mainly controlled by  $\phi$ . The effect of  $\omega$  is less problematic, since the ratio of displacements  $x_{\max}$  and  $z_{\max}$  do not vary in a systematic way with  $\omega$ . However, since  $\omega$  controls the rate at which energy is introduced into the system, both  $\phi$  and  $\omega$  will play a major role in determining the particle motion, as shown in the next section.

Finally, in characterizing the pan motion, tests were conducted to assess the influence of particle bed mass (i.e., the load) on the pan motion. The mass of the unloaded pan is approximately 150 kg. As shown in Fig. 8, it is confirmed that bed masses up to 45 kg have negligible influence on the pan motion, as mentioned in the previous section. Figure 8(a) shows that the bed mass has a negligible influence on the

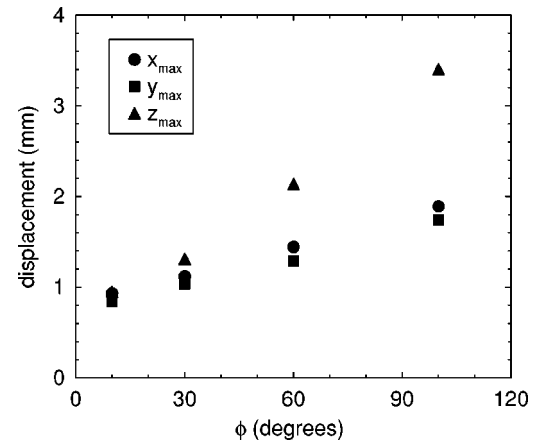


FIG. 5. Maximum displacements  $x_{\max}$ ,  $y_{\max}$ , and  $z_{\max}$  as a function of  $\phi$ . These data are averages over approximately 20 runs over the range of  $\omega$  studied. No systematic variation is observed as a function of  $\omega$ , though individual measurements are scattered about the average by about 15%.

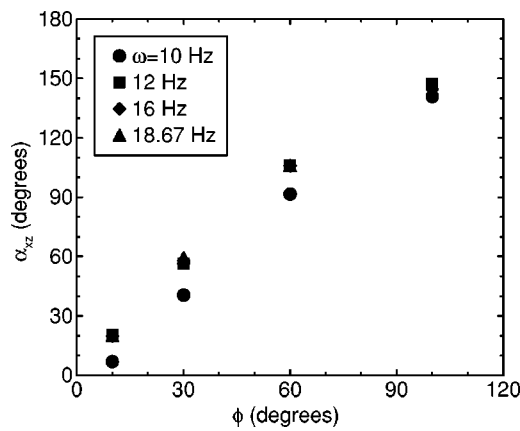


FIG. 6. Phase shift  $\alpha_{xz}$ , as a function of  $\phi$  for various  $\omega$ .

phase shift between the vertical and horizontal motions,  $\alpha_{xz}$ , at different lead angles,  $\phi$ . Figure 8(b) shows that ratios of the maximum amplitudes of the pan motion in the three Cartesian directions are insensitive to bed mass. Figure 8(c) shows that the basic waveform and amplitude of the  $z$  displacement vary little as a function of the bed mass.

An issue related to the effect of the bed mass on the pan motion is the assumption that the stainless steel mesh that forms the bottom of the pan does not flex significantly when impacted by the particle bed. If significant flexing occurred, it might play a role in the observed bed dynamics. A direct measurement of the deformation of the mesh under operating conditions proved difficult. However, visual observation of the mesh, and the fact that the bed dynamics is insensitive to bed mass, suggests that mesh deformation does not play a significant role. To quantify this suggestion, a numerical estimate is made of the maximum deformation of the mesh when subjected to worst-case forces imposed by the moving pan-bed system [13]. The maximum deflection is estimated to be 8 mm, less than the average thickness of a single layer of particles. The ratio of this maximum deflection to the pan diameter is 0.01. This analysis supports the assumption that mesh deformation can be neglected in the present study.

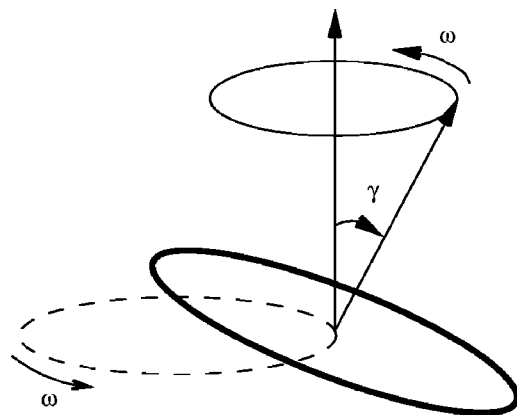
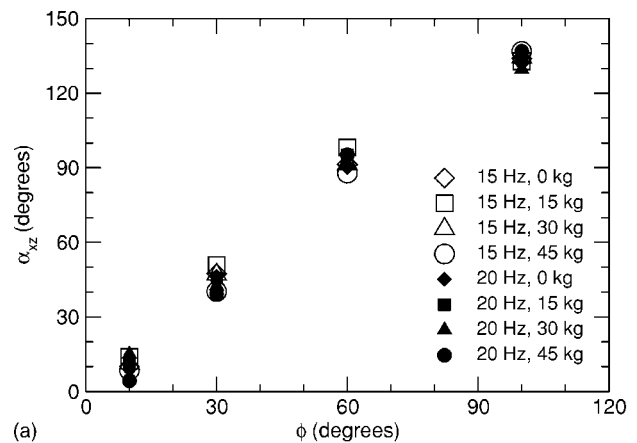
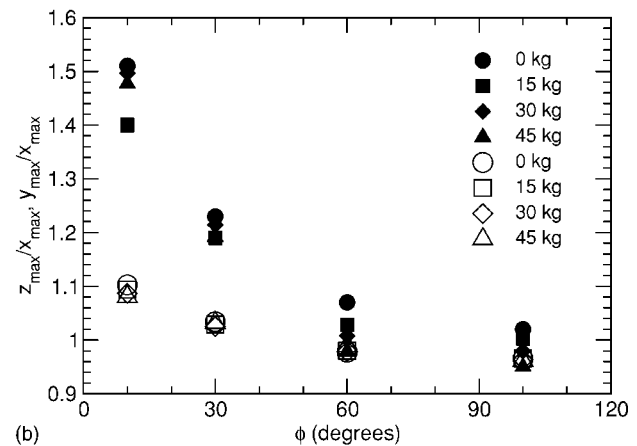


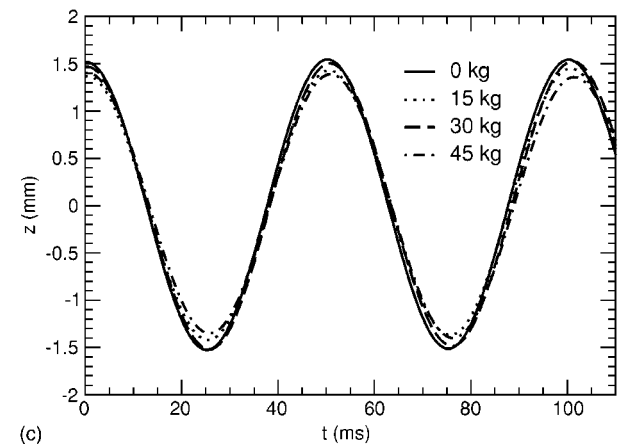
FIG. 7. Schematic representation of the pan motion. The dashed circle represents the orbit of the pan center in the lab frame. The solid circle represents the rim of the pan.



(a)



(b)



(c)

FIG. 8. Influence of particle bed mass on pan motion: (a) phase shift  $\alpha_{xz}$  as a function of lead angle  $\phi$  for different frequencies  $\omega$  and bed masses; (b) maximum displacement ratios  $z_{\max}/x_{\max}$  (filled symbols) and  $y_{\max}/x_{\max}$  (open symbols) as a function of  $\phi$  for  $\omega = 20$  Hz and different bed masses; (c) time series excerpts of the vertical displacement  $z$  as a function of time  $t$ , for  $\phi = 60^\circ$ ,  $\omega = 20$  Hz, and different bed masses.

#### IV. MODES OF PARTICLE BED MOTION

A diagram showing the observed bulk dynamical modes of the particle bed as a function of  $\omega$  and  $\phi$  is shown in Fig. 9(a) for the oblate spheroids, and in Fig. 9(b) for spheres. The bulk motion of the bed is a strong function of  $\omega$ . Four

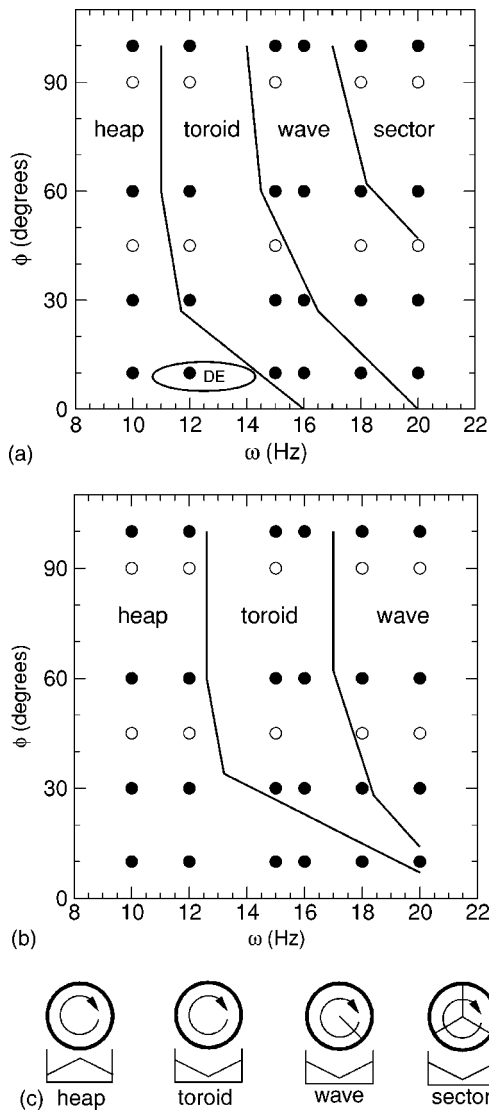


FIG. 9. Diagram identifying the regions of the  $\omega$ - $\phi$  plane in which distinct bulk dynamical modes of the particle bed are observed for (a) oblate spheroids, and (b) spheres. Note that in (a) a region of dynamic equilibrium (“DE”) is observed near  $\phi=10^\circ$ , where the bed does not perform any net rotation about the pan center. This is the boundary region between counterclockwise and clockwise bed rotation (“laps”). Filled circles locate points where both acceleration and visualization measurements were taken; at the open circles, only visualization measurements were taken. Schematic representations of the particle bed shape and motion are shown in (c), for each of the dynamical modes. The upper circles indicate the direction of bed motion as viewed from above the apparatus, while radial lines indicate the presence of surface modulations in the wave and sector cases. The lower pictures represent the shape of the particle bed in a vertical cross section through the center of the pan.

distinct modes of bed motion are observed, here termed “heaping,” “toroidal motion,” “surface waves,” and “sectors.” Each of these is described in detail below. The range of the  $\omega$  at which each of the modes appears depends on the particle shape as can be seen from Fig. 9, but the qualitative behavior of the modes is mostly similar. In the following

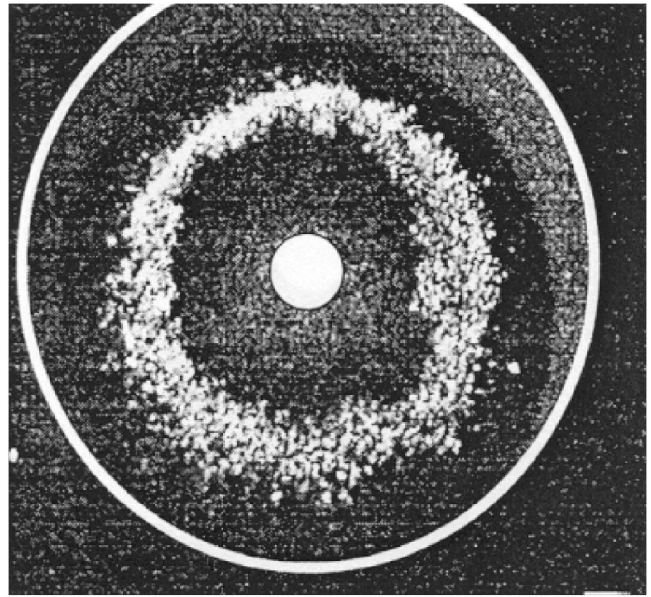


FIG. 10. Fluorescence dye visualization of the particle bed surface motion in the heaping mode. Here the bed mass is 30 kg,  $\phi = 60^\circ$ , and  $\omega = 10$  Hz.

sections, the motion in general is discussed, and differences due to particle shape are identified where appropriate.

### A. Heaping

At the lowest  $\omega$  studied the particles form a heap with an elevated center. The relative particle movement and mixing is very small and the particle bed rotates almost as a solid body. This motion is visualized in Fig. 10. Fluorescent dye is continuously added at a specific location to the surface of the particle bed while in steady-state motion. The subsequent motion of the dyed particles is then captured photographically under ultraviolet light, as shown in Fig. 10. The dyed particles on average undergo a slow processional motion about the pan center. The radial component of the particle motion and the diffusion of particles is negligible. Notably, for most  $\omega$  and  $\phi$ , the particle bed rotates in the direction opposite to that of the orbital motion of the center of the pan; the exceptions to this occur at the lowest  $\phi$  and  $\omega$  studied (e.g.,  $\phi=10^\circ$  and 16 Hz for oblate spheroids), where the rotational directions are the same. The direction of motion of the bed appears to depend on the phase difference  $\alpha_{yz} = \alpha_{xz} - \alpha_{xy}$ . For  $\alpha_{yz} > 0^\circ$ , the bed rotates in the direction opposite of the pan center.

The slope of the particle bed (from the center to the outer edge) initially increases with an increase in  $\phi$ . For example, the bed of oblate spheroids has a nearly flat (horizontal) surface for  $\phi=10^\circ$  and attains the maximum slope at approximately  $\phi=120^\circ$ . As  $\phi$  is further increased, the slope begins to decrease again. Figure 9 schematically shows the cross-sectional shape of the surface during the heaping mode.

The spherical particles move in more tightly packed layers than the oblate spheroids. For  $\phi=100^\circ$ , the layers are very tightly packed and the local arrangement of particles is similar to a close-packed lattice. As  $\phi$  increases, the unifor-

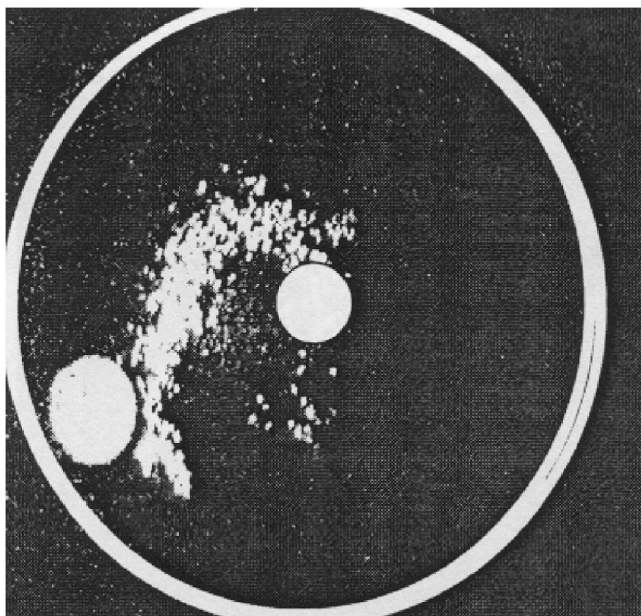


FIG. 11. Fluorescence dye visualization of the particle bed surface motion in the toroidal mode. Particles spiral to the center of the bed along the surface and toward the edges along the pan surface. These reappear at the surface of the bed along the edges. Here, the bed mass is 30 kg,  $\phi=60^\circ$ , and  $\omega=18.67$  Hz. The large white disk near the pan edge is the container from which dye is injected onto the bed surface.

mity of the lattice breaks down. The bed is still tightly packed at  $\phi=100^\circ$ , but more pronounced relative motion of the particles is observed. This change in behavior may be related to the increase of  $z_{\max}$  as  $\phi$  increases (see Fig. 5).

Previous studies of granular matter in vertically excited rectangular containers [15] have shown that relative particle motion is observed when the maximum vertical acceleration exceeds  $1.2g$ . In the present tests, it is found that the local acceleration is below this threshold for  $\omega < 10$  Hz. However, at  $\phi=100^\circ$ , the acceleration at the edge of the pan does approach  $1.2g$ .

**B. Toroidal motion**

As  $\omega$  increases the particle bed undergoes a transformation to a toroidal shape and the particle motion becomes organized. This motion is highly coherent as seen in the fluorescent dye visualizations in Fig. 11. Dye is continuously injected onto the surface of the moving bed. Particles initially on the outer edge move in a spiral motion to the center. Near the center they are subducted and travel outward along the bottom of the pan, to be reentrained along the walls and reappear at the surface at the outer edge of the pan. As seen for the heap, the bulk rotational motion of the bed in the horizontal plane is opposite to that of the center of the pan. The entire particle bed adopts the shape of a torus, through which individual particles move in helical trajectories. The particle motion in a cross-sectional plane through the toroid is depicted schematically in Fig. 12. Note that in addition to the primary circulation roll occupying the center portion of

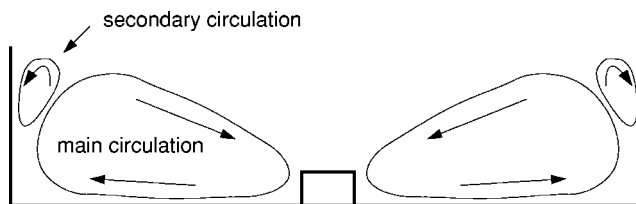


FIG. 12. Schematic of cross section of particle bed, showing direction of particle flows in toroidal motion.

the bed, a small secondary (and counter-rotating) circulation roll forms on the top of the primary one, near the pan wall. The particles move toward the center along the top surface in the primary roll, and toward the wall along the top surface in the secondary roll. The slope of the particle bed surface is greater in magnitude than, and opposite in sign to, that observed for the heap motion.

In this mode of motion, the particle bed is fluidized. The increased agitation results in a relatively rapid diffusion of the particles and a net increase in the mixing rate.

The toroidal motion observed for the circular pan has not been observed in rectangular geometries. An inward spiraling motion has been observed for granular media underneath rotating fluids [10] and the radial segregation of granular mixtures has been observed in rotating cylinders [14]. For vertically excited rectangular beds, stationary convection cells, similar to Rayleigh-Bénard instabilities, are observed [15,16]. For horizontal vibrations, experimental [17] and computational [18] studies have shown that the convective motion consists of granular matter rising to the surface at the middle of the container. In contrast, in the present study, the particles rise along the walls and are subducted at the middle of the pan.

In this context, it is worth noting that the central hub located at the center of the pan does not play a significant role in establishing or maintaining the toroidal motion. Tests confirm that the toroidal motion occurs even if the hub is not present.

**C. Surface waves**

For the two modes described above, the bed height is only a function of the distance from the center of the pan, and the shape of the bed is symmetric about the cylinder axis of the pan. However, for  $\omega > 15$  Hz, crests and troughs appear on the surface of the bed as a function of angular direction around the pan. The crests, or fronts, propagate in the same direction but at a higher speed than the bulk rotation of the bed in the horizontal plane. The speed of the particle fronts initially increases as  $\omega$  increases, but then decreases as  $\omega$  approaches 18 Hz. The amplitude (i.e., the height of the crest above the bed) decreases as  $\omega$  increases. Unfortunately, this motion is very difficult to capture on still media.

The individual particle trajectories can still be described as helical. The motion of the crests appears to be similar to a traveling wave.

**D. Sectors**

For  $18 < \omega < 20$  Hz, the motion of crests on the surface of the bed becomes nearly stationary, dividing the bed into

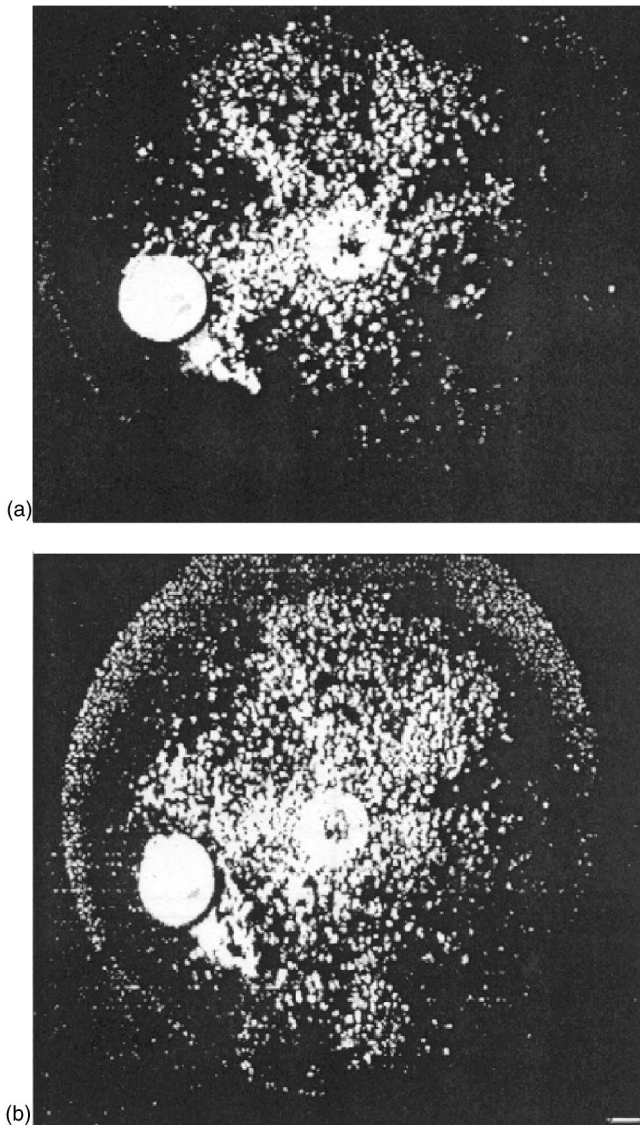


FIG. 13. Two fluorescence dye visualizations of sectors. The sectors can be visualized because the particles located on the crests dry faster than those in the trough and lose fluorescence. The large white disk near the pan edge is the container from which dye is injected onto the bed surface.

well-defined “sectors.” These sectors are visualized using fluorescent dye in Fig. 13. The number of sectors present in the bed is found to be a function of  $\phi$  and  $\omega$ . The sectors are stable and easily recognized for the oblate spheroids. However, for the spherical particles, stationary sectors are more difficult to achieve and could not be reliably reproduced.

Although the general bulk motion of the particles remains helical, the sector mode is distinct from the toroidal mode. Defining the general direction of the precessional motion as streamwise, it is seen that the particles on the upstream side of the crests are drawn into the bed, while on the downstream side particles emerge on the surface. The upstream particles have been exposed to air for a longer period and have dried, causing the dye to lose fluorescence. The upstream side of the crests thus appear darker than the downstream side, yielding the “rays” seen in Fig. 13. Also, in the sector mode, the

secondary circulation roll near the wall that was characteristic of the unmodified toroidal mode of motion could not be observed.

As  $\omega$  is further increased to 26 Hz, the toroidal motion (without sectors or surface waves) is recovered. Unfortunately, the mechanical limitations of the apparatus did not allow testing at larger  $\omega$ .

## V. DISCUSSION

### A. Rotation of the particle bed in the horizontal plane

The direction of rotation of the particle bed in the horizontal plane is generally opposite to that of the center of the pan. This behavior is initially counterintuitive, and explaining it requires a detailed understanding of the interplay between the bed motion, the pan orientation, and the horizontal and vertical components of the pan motion.

A crucial element for resolving this behavior is to determine the shape and motion of the zone of contact of the particle bed with the pan. Because the pan is tilted away from the vertical at all times during its motion, it seems likely that only a particular sector of the bed is in contact with the pan at any given time; and that the angle at which maximum contact occurs between the bed and the pan rotates about the pan center at the same frequency  $\omega$  as the pan center itself. If this is true, at least two contributions to the mechanism of bed rotation can be envisioned.

(i) *Deflection by the pan surface.* Consider an element of the pan surface within the zone of contact between the pan and bed. At any given time, the normal to this surface element can be decomposed into vertical, radial, and tangential components, defined with respect to a cylindrical coordinate system in the lab frame. Particles striking this surface element will tend to be deflected according to the orientation of the surface normal. In the absence of other mechanisms, a net rotational motion about the pan center will occur if the direction of the tangential component remains constant. This will be true if (as assumed above) the zone of particle-bed contact rotates around the pan bottom at the same frequency as the pan itself precesses. The direction of this bed rotation will be independent of the rotational direction of the pan center, since it depends on the (presently unknown) location of the region of particle-bed contact. Hence, the bed could well be set into a rotational motion opposite to that of the pan center (Fig. 14).

(ii) *Entrainment by the pan surface.* Independent of the above mechanism, the effect of friction between the particles and the pan bottom should also be considered. As described in Sec. II, the pan bottom consists of a metal screen, and so is “rough” on the scale of the particles themselves. Consider the same surface element in the contact zone as discussed above, but instead of its orientation, consider its velocity vector decomposed into vertical, radial, and tangential components. This rough surface element will tend to transfer momentum to particles in contact with it according to the direction of its velocity. Analogous to the reasoning given above, particles in the contact zone will be subjected to a constant tangential surface velocity, yielding a net rotation of the bed about the pan center. Also as above, the direction of

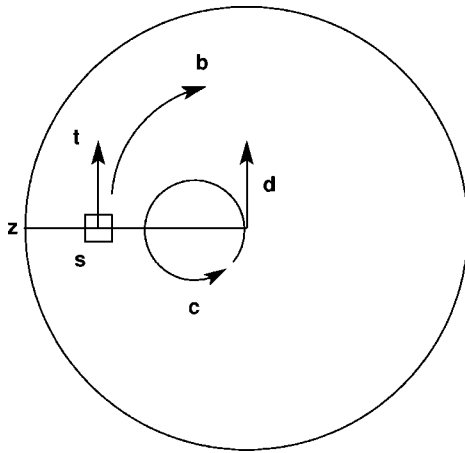


FIG. 14. Schematic illustration of scenarios for explaining direction of bed rotation. The large circle represents the edge of the pan as viewed from above.  $c$  is the circular trajectory of the center of the pan as seen in the lab frame, while  $d$  is the instantaneous direction of motion of the pan center at the moment depicted.  $s$  is a surface element of the pan bottom along the direction  $z$  of the zone of maximum contact between the pan and the bed. Scenario (i): If the vector  $t$  represents the tangential component of the normal to  $s$ , then particles will be deflected along  $t$ , leading to bed rotation in the direction  $b$ , opposite to  $c$ . Scenario (ii): If the vector  $t$  represents the tangential component of the velocity of  $s$ , then particles will be “dragged” in the direction of  $t$ , leading to bed rotation along  $b$ , again opposite to  $c$ .

the resulting bed rotation will be independent of that of the pan center, and so it should be possible to establish conditions where these rotations would be opposite in direction (Fig. 14).

Whatever the underlying mechanism, an explanation can be tested against the observed dependence of the motion on the control parameters. For example, the speed of rotation of the bed in the horizontal plane depends on the phase difference between the horizontal and vertical pan motions,  $\alpha_{xz}$ . For  $0^\circ < \alpha_{xz} < 180^\circ$ , the particles are observed to move in the direction opposite to that of the bed. However, as mentioned earlier, it is indeed possible to realize conditions where the bed rotates in the same direction as the pan, when  $\phi$  is changed such that  $\alpha_{xz} < 0^\circ$ .

In addition, the rotational speed of the bed in the horizontal plane increases with  $\omega$ . Furthermore, as shown in Fig. 15, the rotational speed is found to be greatest when  $\alpha_{xz} = 90^\circ$ , corresponding to  $\phi = 60^\circ$  (see Fig. 6).

Elucidation of these phenomena requires information on the (time-dependent) location of contact between the pan and the bed. This information is not available in the present measurements. These questions are being explored through further experiments, and through computer modeling.

**B. Radial motion of the particles**

Understanding the radial motion of the particle bed also requires a careful consideration of the bed and pan motions. In the toroidal mode, the particles move along the bottom of the bed toward the wall, and then back toward the center of

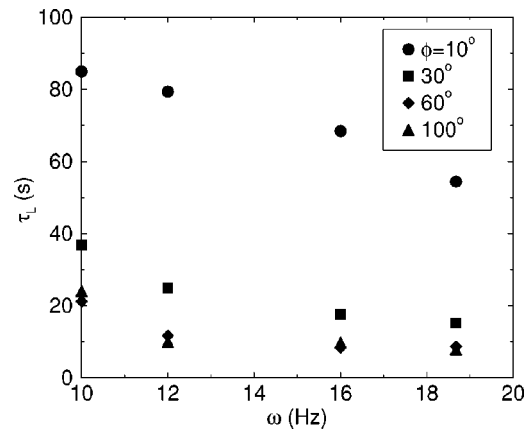


FIG. 15. A plot of the average lap time  $\tau_L$  in seconds.

the pan along the top surface of the bed. It seems likely that the motion of particles near the pan bottom is due to their being entrained by the motion of the pan surface itself. The inward motion of particles on the bed surface, where the particle packing is looser, may be dominated by gravity-induced downward flow toward the bed center, where the bed depth is smallest. However, these possible explanations do not fully elucidate the origin of the toroidal shape adopted by the bed in this mode, and so further study of this behavior is needed.

The ratio of the rotational speed of the particle bed in the horizontal plane to the radial speed is shown in Fig. 16. To measure this, the motion of color-tagged particles is observed in steady state. The average time  $\tau_L$  required for a tagged particle to complete one circuit (a “lap”) around the pan in the horizontal plane is measured; the average time  $\tau_O$  required for a tagged particle to complete one circuit (an “over”) from the center of the pan to the outside edge and back to the center is also measured. The ratio  $\tau_L/\tau_O$  is shown in Fig. 16.

In the heaping mode the radial motion is negligible, as indicated in Fig. 10. When the vertical acceleration is sufficiently high to fluidize the particles (i.e., the particles are not in continuous contact with the pan surface), the radial and horizontal rotational speeds of the particles are found to de-

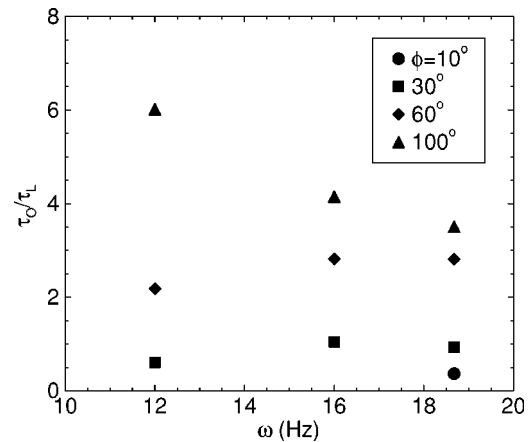


FIG. 16. A plot of the overs-to-lap ratio for the oblate spheroids.

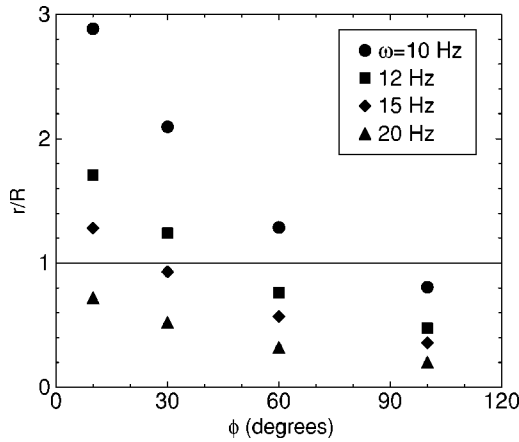


FIG. 17. Critical radius at which the vertical acceleration is  $g$  as a function of  $\phi$ .

pend only on the phase difference between the horizontal and vertical pan motions. This is shown in Fig. 16: as  $\omega$  is increased,  $\tau_O/\tau_L$  approaches a constant value, which is a function of  $\phi$ .

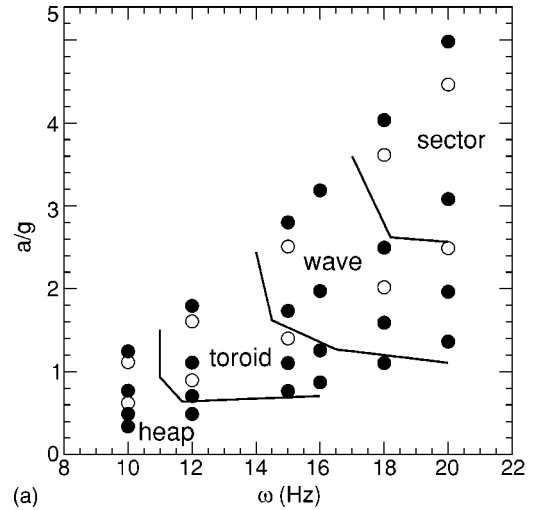
### C. Critical acceleration and fluidization

The data in Fig. 5 are used to determine the critical radius, shown in Fig. 17, at which the maximum vertical acceleration exceeds  $g$ . For  $\phi=10^\circ$  and  $\omega < 18$  Hz, the vertical acceleration is less than  $g$  and the particles at the bottom of the bed are constantly in contact with the pan surface. This is consistent with the radial motion of the particle bed being negligible, as indicated in Fig. 9. Based on the model motion in Eqs. (1)–(3), for  $\omega=20$  Hz, the vertical acceleration exceeds  $g$  when  $r_p/R > 0.81$ . Under these conditions the toroidal motion is induced, in which case an overs-to-lap ratio could be clearly defined (Fig. 16). As  $\phi$  increases, the critical value of  $g$  occurs in the bed at smaller  $\omega$ , in agreement with the observations summarized in Fig. 9.

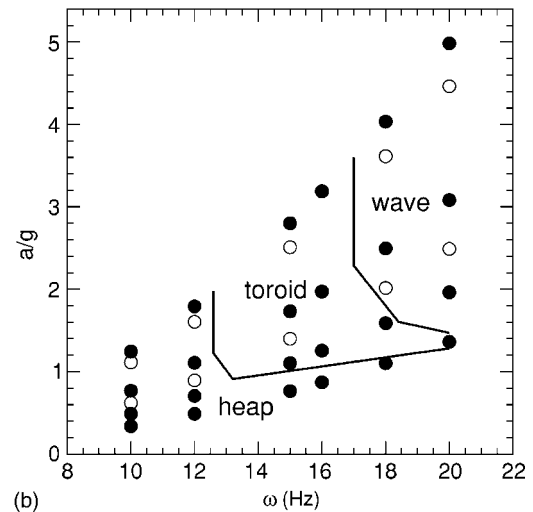
When the maximum vertical acceleration in the pan is much less than  $g$ , the tilting motion of the pan induces only a rotational motion of the bed in the horizontal plane, since the particles at the bed bottom remain in constant contact with the pan surface and the net radial bed motion is zero. When the maximum acceleration approaches or exceeds  $g$ , the particles at the bottom of the bed start to be lifted above the pan surface, allowing a net radial displacement to be induced, and leading to the toroidal motion. For  $\phi > 30^\circ$  and  $\omega > 16$  Hz, the particle bed is fluidized over most of the pan area. This is the range of  $\omega$  in which the “wave” and “sector” modes are seen.

Similar information on the influence of acceleration is conveyed in Fig. 18, which shows the same information as in Fig. 9, reparametrized so that  $\phi$  is replaced by the corresponding value of  $a/g$ , where  $a$  is the maximum acceleration occurring at  $r=R$ . This provides a plot more comparable to those given in other studies where  $\omega$  and acceleration are the natural control variables.

Both Figs. 17 and 18 show that, at high  $\omega$ , the heap mode crosses over to the toroidal mode as  $a$  approaches  $g$ . How-



(a)



(b)

FIG. 18. Same information as is plotted in Fig. 9, but with  $\phi$  replaced by the ratio  $a/g$  where  $a$  is the maximum acceleration occurring at  $r=R$ .

ever, the high- $\omega$  crossover seems to occur for  $a < g$ , and lower than the critical acceleration of  $1.2g$  reported for fluidization of granular matter in other studies [19–21]. This suggests that in the toroidal mode, the entire particle bed need not be fluidized in order to initiate the radial circulation of particles. At the same time, Fig. 18 shows that the heap mode survives even when  $a > g$  for the lowest  $\omega$ . The mechanism for the heap-to-toroidal crossover is therefore not entirely controlled by  $a$ .

It is worth noting the differences between the heap mode observed here, and heaping regimes found in experiments employing vertical vibrations only, such as those described in Refs. [22–24]. These earlier studies observe heaps that form only when the acceleration is greater than  $g$ , and which involve some form of convection, due either to the interaction of an interstitial gas (air) with the particle bed, or due to particle flow imposed by the vertically moving sides of the container. In the present study, the heap mode is observed for accelerations less than  $g$ , and no observable convection occurs. It should also be noted that the particle sizes considered here are much larger than those used in the previous studies

of heap formation cited above. It is therefore unlikely that hydrodynamic forces on the particles due to the movement of an interstitial gas play a significant role in the present heaping mechanism. Visual observation of the heap suggests that the driving mechanism underlying its formation is simply due to the horizontal vibrations of the vertical sides of the pan. The horizontal vibrations of the sides drive nearby particle away, while particles nearer the center are relatively unaffected. As a result, the particles pile up into a heap away from the pan sides.

As described in the previous sections, the toroidal mode is driven by the combined effects of the rotational motion of the bed and the radial circulation. Both of these motions are forced flows controlled by the particle-wall interactions, although, as stated earlier, identification of the precise nature of the forcing requires future work. Nonetheless, the toroidal mode arises as  $a$  approaches  $g$ , and so the instability underlying the heap-to-toroidal crossover may belong to the same family of instabilities which occur in vibratory conveyors and similar systems in which forced flows are induced by a combination of vertical and horizontal vibrations.

The heap-to-toroidal crossover is the most prominent dynamical change observed in the system over the observed range. The wave and sector regimes described in Secs. IV C and IV D are by comparison more subtle variations of the general toroidal motion, and the driving mechanisms by which they form are the least clear of the modes considered

here. The apparatus and instrumentation used here do not provide any information on particle motion, or particle-wall forces, inside the particle bed, so it is not possible to present a complete description of the phenomena that generate the surface features found in the wave and sector regimes. It should be noted that the surface modulations in these regimes are not subharmonic parametric waves [7,25–28]: the surface modulations do not cycle between peaks and troughs and back again. Rather, visual observation indicates that convective flow is involved, especially in the sector regime (see Sec. IV D). It may be that the bed is segmenting into a series of convection cells with rotational axes oriented radially from the pan center.

Given the apparent differences between the dynamical modes described here, and those reported for vertically vibrated granular matter, further investigation is needed. Computer simulations are currently under way to further elucidate the origin of the behavior described here [29].

#### ACKNOWLEDGMENTS

We thank Materials and Manufacturing Ontario and NSERC (Canada) for financial support. P.H.P. also acknowledges support from the Canada Research Chairs program. We also acknowledge valuable discussions with K. Bevan, J. J. Drozd, and E. B. Smith.

- 
- [1] H. M. Jaeger and S. R. Nagel, *Science* **255**, 1523 (1992).
  - [2] D. Bideau and J. Dodds, in *Physics of Granular Media*, Les Houches Series (Nova Science, Commack, NY, 1991).
  - [3] *Granular Matter: An Interdisciplinary Approach*, edited by A. Mehta (Springer-Verlag, New York, 1994).
  - [4] H. M. Jaeger, S. R. Nagel, and R. P. Behringer, *Rev. Mod. Phys.* **68**, 1259 (1996).
  - [5] H. M. Jaeger, S. R. Nagel, and R. P. Behringer, *Phys. Today* **49**(4), 32 (1996).
  - [6] P.-G. de Gennes, *Physica A* **261**, 267 (1998).
  - [7] C. Wassgren, C. E. Brennen, and M. L. Hunt, *J. Appl. Mech.* **63**, 712 (1996).
  - [8] C. Bizon, M. D. Shattuck, J. B. Swift, W. D. McCormick, and H. L. Swinney, *Phys. Rev. Lett.* **80**, 57 (1998).
  - [9] S. G. K. Tennakoon and R. P. Behringer, *Phys. Rev. Lett.* **81**, 794 (1998).
  - [10] M. A. Scherer, T. Mahr, A. Engel, and I. Rehberg, *Phys. Rev. E* **58**, 6061 (1998).
  - [11] Part of this research was conducted in collaboration with a private sector firm with a proprietary commercial interest in the results involving the oblate spheroid particles. A nondisclosure agreement precludes us from identifying the name of this firm, or the chemical composition of the ellipsoidal particles.
  - [12] The nylon spheres are “QK grade III matte finish nylon balls” obtained from Machining Technologies, Elmore, OH.
  - [13] We estimate the maximum deflection of the mesh by solving an appropriate set of coupled force balance equations. Each wire is modeled as a member under tension supported at the points of intersection with other wires. The dilation of the wires is approximated using Hooke’s law, with parameters appropriate for stainless steel. The system of equations is solved computationally. Conservative assumptions are made: (i) the total bed mass is distributed over only half of the mesh, since the mesh is moving away from the bed on the other side; (ii) the height of the bed varies linearly, increasing toward the pan edge; (iii) the vertical acceleration varies linearly with the radial position, as found in the experiments; (iv) the maximum force is equivalent to that produced by an acceleration twice as large as the local peak acceleration, to account for impact loading associated with the bed.
  - [14] D. V. Khakhar, J. J. McCarthy, and J. M. Ottino, *Phys. Fluids* **9**, 3600 (1997).
  - [15] Y. Lan and A. D. Rosato, *Phys. Fluids* **9**, 3615 (1997).
  - [16] J. B. Knight, E. E. Ehrichs, V. Yu. Kuperman, J. K. Flint, H. M. Jaeger, and S. R. Nagel, *Phys. Rev. E* **54**, 5726 (1996).
  - [17] S. G. K. Tennakoon, L. Kondic, and R. P. Behringer, *Europhys. Lett.* **45**, 470 (1998).
  - [18] C. Saluena and T. Poschel, *Eur. Phys. J. E* **1**, 55 (2001).
  - [19] P. Evesque and J. Rajchenbach, *Phys. Rev. Lett.* **62**, 44 (1989).
  - [20] P. Evesque, E. Szmatala, and J. P. Denis, *Europhys. Lett.* **12**, 623 (1990).
  - [21] P. Evesque, *Contemp. Phys.* **33**, 245 (1992).
  - [22] C. Laroche, S. Douady, and S. Fauve, *J. Phys. (France)* **50**, 699 (1989).
  - [23] E. Clement, J. Duran, and J. Rajchenbach, *Phys. Rev. Lett.* **69**, 1189 (1992).

- [24] E. Falcon, K. Kumar, K. M. S. Bajaj, and J. K. Bhattacharjee, *Phys. Rev. E* **59**, 5716 (1999).
- [25] S. Douady, S. Fauve, and C. Laroche, *Europhys. Lett.* **8**, 621 (1989).
- [26] F. Melo, P. B. Umbanhowar, and H. L. Swinney, *Phys. Rev. Lett.* **72**, 172 (1994).
- [27] F. Melo, P. B. Umbanhowar, and H. L. Swinney, *Phys. Rev. Lett.* **75**, 3838 (1995).
- [28] T. H. Metcalf, J. B. Knight, and H. M. Jaeger, *Physica A* **236**, 202 (1997).
- [29] O. Baran, J. J. Drozd, P. Sistla, R. J. Martinuzzi, and P. H. Poole (unpublished).